High-fidelity Aeroelastic Analysis of Rotor Blade using Three-dimensional Finite Element Formulation and Panel Method

Seongwoo Cheon, Dept. of Aerospace Engineering, Jeonbuk Nat'l Univ., Jeonju, South Korea
Byeonju Kang, Dept. of Aerospace Engineering, Jeonbuk Nat'l Univ., Jeonju, South Korea
Sangmin Son, Dept. of Mechanical Aerospace Engineering, Gyeongsang Nat'l Univ., Jinju, South Korea
Salang Lee, Dept. of Mechanical Aerospace Engineering, Gyeongsang Nat'l Univ., Jinju, South Korea
Haeseong Cho, Dept. of Aerospace engineering, Jeonbuk Nat'l Univ., Jeonju, South Korea
Hakjin Lee, Dept. of Mechanical Aerospace Engineering, Gyeongsang National Univ., Jinju, South Korea
Youngjung kee, Korea Aerospace Research Institute, Daejeon, South Korea

Abstract

Three-dimensional (3D) solid finite element analysis (FEA) is developed to perform a high precision aeroelastic analysis of a rotor blade. This study is focus on geometrically nonlinear problems with linear elastic material properties. The 3D finite element (FE) formulation is based on updated Lagragian approach to estimate the large rotations and displacements. The 20-nodes solid element with eight Gaussian integration points is employed to construct the FE model of rotor blade to prevent the element locking and hourglass modes. Moreover, the method to calculate the sectional loads of structure is presented based on force balance method. To do this, the internal force is adopted. For high-precision aeroelastic analysis, the 3D FEA is coupled with source-doublet panel method and vortex particle hybrid method using loosely coupling method to predict the aeroelastic behavior and blade sectional loads. The multi-purpose unmanned helicopter (MPUH) blade developed by Korea Aerospace Research Institute (KARI) is employed as a validation of the present analysis results. Herein, sectional load observation from experiments and aeroelastic analysis in hover flight condition using CAMRAD II are considered. Accuracy of the present high-precision analysis is evaluated by comparing prediction of performance, structural behaviors, and sectional load results.

1. INTRODUCTION

The aeroelastic analysis of rotorcraft system involves the interacting elastic components such as blades and rotors etc. and they exhibit nonlinear structural behavior during flight operations due to the rotating inertial force and aerodynamic loads. Therefore, it is essential to accurately predict rotor blade vibration and structural loads.

Typically, the comprehensive analysis in rotorcraft involves two-dimensional cross section finite analysis, to calculate the spanwise structural properties of the blade, and one-dimensional (1D) beam element or 1D geometrically exact beam analysis (Ref. 1-2). The method is efficient and accurate as long as the cross-sections are small compared to the wavelength of deformation along the beam (Ref. 3). However, 1D beam based analysis faces several limitations: It cannot model the three-dimensional (3D) hub structure of advanced rotors and airfoil chordwise flexibility, which may be important to advanced smart rotors. Although it is possible to analyze the complex rotor blades due to development of beam-based method, it relies on prior experimental measurements and simplifications of the actual structure to model the blade root conditions. Therefore, 3D finite element-based rotorcraft analysis is needed to overcome these limitations of the conventional approaches although computationally intensive. The primary benefit of aeroelastic analysis using 3D FEA and panel method is not only increased fidelity but also an increase in capability and scope of rotor blade modeling, enabling the prediction of 3D stresses and strains in various flight conditions. Yeo and Truong (Ref. 4-5) performed 3D finite element analysis of rotating beams and blades. Kee and Shin (Ref. 6) analyzed the dynamic characteristics of rotating blades using a shell-solid element, which is same nodes and degree of freedom configuration of solid element, but shell-like behavior in the thickness direction is taken into consideration. In their works, they compared natural frequencies predicted by 3D analysis to those from beam analysis. For next generation 3D rotor structural dynamic analysis, X3D was developed by the US Army Aviation Development Directorate and the University of Maryland, College of Park, which is a 3D solid finite element analysis- and multibody dynamics-based rotor structural solver (Ref. 7). It has been employed to predict the dynamic characteristics of various rotor blades such as single rotor (Ref. 8), coaxial rotor (Ref. 9), and tilt rotor (Ref. 10).

Zhu et al. employed the panel/vortex particle hybrid method to the blade unsteady aerodynamic loads. In their work, the hybrid method was coupled with the multibody dynamic code MBDyn (Ref. 12), and the results matched well with experimental data and CFD results both in the hover and forward flight conditions (Ref. 13). In this study, the aerodynamic forces on a rotor are predicted using source-doublet panel method coupled with vortex particle method (VPM). This method, in which the airfoil involved in the rotor blade is divided into upper and lower panels, can predict airloads for complex blade geometry due to consider the thickness and chordwise effect of the rotor blade. Additionally, compared to computational fluid dynamics (CFD) analysis, it has the advantage of providing rapid results with reasonable fidelity, although it has limitations in considering viscous and compressible effects (Ref. 11).

Moreover, the 3D solid finite element analysis (FEA) including the computation of sectional blade loads from 3D structural analysis is developed for rotorcraft dynamics with emphasis on the geometrical nonlinearity of rotor blades. Comparisons between multi-purpose unmanned helicopter (MPUH) data developed by Korea Aerospace Research Institute (KARI) and results of aeroelastic analysis coupling panel/vortex hybrid method with 3D FEA are presented.

2. METHODOLOGY

2.1. 3D finite element formulation

The 3D finite element formulation is based on well-established procedures (Ref. 15-16). In this study, the updated Lagrangian description of the motion of solid bodies undergoing the geometrical nonlinear behavior is adopted. Therefore, the current configuration is used as reference frame to measure the physical properties, and the Cauchy stress and engineering strain should be used. The three configurations of body are considered: undeformed configuration C_0, the last known configuration C_1, and the deformed current configuration C_2.

The updated Lagrangian formulation is based on virtual work per unit deformed volume. The strain energy of the deformed structure can be calculated using the engineering strain and Cauchy stress with integration over deformed volume is simply as

$$\delta U = \int_V \sigma_{ij}\delta\varepsilon_{ij}dV \tag{1}$$

It is noted that the configuration C_2 is a function of displacement, and the nonlinear analysis will be difficult because the configuration C_2 is not known. Therefore, the updated Lagrangian formulation could be easily derived using the strain and stress measured in the configuration C_0.

The deformed coordinates of a material point at any instant are

$$x_i = x_i^0 + u_i(x_i^0) \tag{2}$$

where x_i^0 and u_i denote the undeformed coordinates and the displacement, respectively. The deformation gradient of the point with respect to its undeformed configuration is

$$F_{ij} = \frac{\partial x_i}{\partial x_j^0} \tag{3}$$

The element of Green-Lagrange strain tensor in the configuration C_2 is defined by

$$\begin{aligned}\epsilon_{ij} &= \frac{1}{2}\left(F_{ki}^T F_{kj} - 1\right)\\ &= \frac{1}{2}\left(\frac{\partial u_i}{\partial x_j^0} + \frac{\partial u_j}{\partial x_i^0} + \frac{\partial u_k}{\partial x_i^0}\frac{\partial u_k}{\partial x_j^0}\right)\end{aligned} \tag{4}$$

where x_i^0 and u_i are the Cartesian coordinates and displacement components, respectively.

The strain energy for elastic structure with integration over the undeformed volume is given by

$$\delta U = \int_{V_0} S_{ij}\delta\epsilon_{ij}dV_0 \tag{5}$$

where S_{ij} denotes the 2nd Piola-Kirchhoff stress and $\delta\epsilon_{ij}$ is the variation of Green-Lagrange strain tensor. Both are physical quantities corresponding to the configuration C_2 but referred to the configuration C_0.
For nonlinear analysis, the incremental procedure is followed. The variation in the strain energy is expressed in terms of incremental deformations measured in configuration C_1. The Green-Lagrange strain increment tensor are defined as

$$\begin{aligned}\Delta\epsilon_{ij} &= \frac{1}{2}\left(\frac{\partial\Delta u_i}{\partial x_j^0} + \frac{\partial\Delta u_j}{\partial x_i^0} + \frac{\partial u_k}{\partial x_i^0}\frac{\partial\Delta u_k}{\partial x_j^0}\right. \\ &\qquad \left. + \frac{\partial\Delta u_k}{\partial x_i^0}\frac{\partial u_k}{\partial x_j^0}\right) + \frac{1}{2}\frac{\partial\Delta u_k}{\partial x_j^0}\frac{\partial\Delta u_k}{\partial x_j^0} \\ &= \Delta e_{ij} + \Delta\eta_{ij}\end{aligned} \tag{6}$$

where the linear and nonlinear strains are separately denoted as e_{ij} and η_{ij}. The variations follow

$$\delta\Delta\epsilon_{ij} = \delta\Delta e_{ij} + \delta\Delta\eta_{ij} \tag{7}$$

where

$$\begin{aligned}\delta\Delta e_{ij} &= \frac{1}{2}\left(\frac{\partial\delta\Delta u_i}{\partial x_j^0} + \frac{\partial\delta\Delta u_j}{\partial x_i^0} + \frac{\partial u_k}{\partial x_i^0}\frac{\partial\delta\Delta u_k}{\partial x_j^0}\right. \\ &\qquad \left. + \frac{\partial\delta\Delta u_k}{\partial x_i^0}\frac{\partial u_k}{\partial x_j^0}\right)\end{aligned} \tag{8}$$

$$\delta\Delta\eta_{ij} = \frac{1}{2}\left(\frac{\partial\Delta u_k}{\partial x_i^0}\frac{\partial\delta\Delta u_k}{\partial x_j^0} + \frac{\partial\delta\Delta u_k}{\partial x_i^0}\frac{\partial\Delta u_i}{\partial x_j^0}\right) \tag{9}$$

The strain-stress relationship could be described using the constitutive equation as shown in Eq 00. where C_{ijkl} is the material constitutive tensor in configuration C_0, and ΔS_{ij} is the incremental 2nd Piola-Kirchhoff stress.

$$\Delta S_{ij} = C_{ijkl}\Delta\epsilon_{kl} \tag{10}$$

Using the Eq. (8), (9), and (10), the variation in strain energy is written as

$$\delta U = \int_{V_0} C_{ijkl}\Delta\epsilon_{kl}\delta\Delta\epsilon_{ij}dV_0 + \int_{V_0} S_{ij}\delta\Delta\epsilon_{ij}dV_0 \tag{11}$$

The Eq. 00 include the nonlinearity involved in the displacement, which makes the equation of motion described later difficult to solve directly. By employing the assumption $\Delta\epsilon_{ij} \cong \Delta e_{ij}$, the variation in strain energy can be written as

$$\delta U = \int_{V_0} \left(C_{ijrs}e_{rs}\delta e_{ij} + S_{ij}\delta\eta_{ij} + S_{ij}\delta e_{ij}\right)dV_0 \tag{12}$$

To calculate the strain energy in configuration C_2, the strain and stress are measured at the configuration C_2. Therefore, the linearized strain energy formulation should be converted into a formulation using engineering strain and Cauchy stress. The relationship between engineering strain and Green-Lagrange strain is obtained from Equation 00 and is written as

$$\epsilon_{ij} = F_{ki}\varepsilon_{kl}F_{lj} \tag{13}$$

Moreover, the Cauchy stress is obtained using the relationship between 1st Piola-Kirchhoff stress and 2nd Piola-Kirchhoff stress and is written by

$$\sigma_{ij} = \frac{1}{J}FSF^T \tag{14}$$

where J is the determinant of deformation gradient F_{ij}. Substituting Equations 00 and 00 into the Equation 00, the variation in strain energy is

$$\delta U = \int_V \left(c_{ijrs}e_{rs}\delta e_{ij} + \sigma_{ij}\delta\eta_{ij} + \sigma_{ij}\delta e_{ij}\right)dV \tag{16}$$

where

$$\delta\Delta\eta_{ij} = \frac{1}{2}\left(\frac{\partial\Delta u_k}{\partial x_i}\frac{\partial\delta\Delta u_k}{\partial x_j} + \frac{\partial\delta\Delta u_k}{\partial x_i}\frac{\partial\Delta u_i}{\partial x_j}\right) \tag{17}$$

$$c_{ijkl} = \frac{1}{J}F_{ir}F_{js}F_{km}F_{ln}C_{rsmn} \tag{18}$$

The c_{ijkl} is the 4th-order constitutive tensor in configuration C_2.
The kinetic energy of rotating blades affects stiffness and inertial force, known as spin softening and centrifugal force. The kinetic energy can are expressed as

$$T = \int_V \rho v_i^2 dV \tag{19}$$

where $\ddot{r}$ and δr are the acceleration and virtual displacement of a material point on the blade relative to an inertial frame. The position vector r from origin of the inertial frame to deformed geometry is

$$r = h + x + u \tag{20}$$

where h is the translational offsets of the global frame (non-inertial frame) evaluated from the inertial frame, which is considered as the rotating center of blade. x and u are position vector and displacement vector, respectively, relative to inertial frame.
Therefore, the components of the time derivative of position vector r relative to inertial frame are

$$v = \dot{r} + \tilde{\omega}r \tag{21}$$

$$a = \ddot{r} + \tilde{\omega}\dot{r} + \dot{\tilde{\omega}}r + \tilde{\omega}\tilde{\omega}r \tag{22}$$

where v and a are velocity vector and acceleration vector of an arbitrary point relative to inertial frame. ω is a rotating velocity of inertial frame. The variational form of kinetic energy can be written as

$$\delta T = \int_V \rho \delta u \left(D_u \ddot{u} + D_v \dot{u} + D_w u + D_f \right) dV \qquad (23)$$

where the third and fourth terms on the right-hand side are the spin softening effect and centrifugal force, respectively. The details of coefficients D_u, D_v, and D_w associated with $\ddot{u}$, $\dot{u}$, and u are described in Ref. 6.

For a static problem of rotating blade, given a prescribed, deformation independent external loading, the equation of motion can be written as Eq. 00, and then solved using the Newton-Raphson method.

$$\delta U - \delta T = \delta W_E \qquad (24)$$

where δW_E is the work done by external forces, and the time-variant terms in δT are equal to zeros.

The analysis of rotor blades dominated by bending motion involving thin structures using 3D elements suffers from severe stiffening known as element locking. Moreover, the lower-order element with reduced integration method for computational cost efficiency may leads to element distortions that have zero strain energy known hourglass modes. A simple and effective way to prevent these problems is to use higher order elements and reduced integration method. Therefore, the twenty nodes solid element and eight integration points are considered in this study as shown in Figure 1.

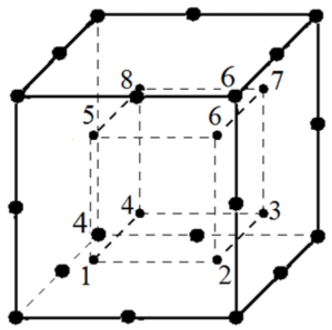

Figure 1: 20-nodes solid element with eight Gaussian integration points

2.2. Sectional loads

Because 3D FEA generates detailed strain and stress distribution over the entire rotor blade, the way to calculate the sectional loads can be considered by integrating sectional stresses. However, fine mesh generation at pre-processing are required to accurately predict stress over the entire blade and causes an increase in computational cost. In this study, a more efficient approach based on force balance method is proposed to validate the prediction of proposed structural solver. This method obtains sectional loads between applied forces and inertial forces acting on the segment to one side of x_L.

First, the internal forces calculated during the structural analysis could be used, which are applied to each node in the global frame as shown in Eq. (5).

$$F^{int} = \int_V \sigma_{ij,i} dV \qquad (26)$$

They need to be transformed from global frame to bent cross section frame using the rotational operator (Ref. 17). The section loads calculated using the internal forces on inboard and outboard of x_L are

$$F = C^{BA} \sum_{x \le L} W F^{int} \qquad (27)$$

$$M = C^{BA} \sum_{x \le L} W(x - r) \times F^{int} \qquad (28)$$

where C^{BA} is a rotation operator mapping from global frame to bent cross section frame, and notation A and B are global coordinate and cross section coordinate, respectively. x and r are the position vector of node and the position vector to evaluate moments. W is a weighting function to gives at the blade tip the same result as the nodal reaction.

$$W = \begin{cases} x_L/L, & x > x_L \\ x_L/L - 1, & x \le x_L \end{cases} \qquad (29)$$

2.3. Panel/Vortex particle hybrid method

In this study, the aerodynamic analysis employs the panel/vortex particle hybrid method, where the panel method is employed to simulate the rotor blade surfaces and close wakes, and VPM is used to model the far wake. The panel method divides the blade surface and close wakes into quadrilateral panels with constant strength. The sum of velocity potential is equal to the sum of constant strength of source σ and doublet μ. Considering the potential influence coefficients on the source and doublet between each discretized panel and wakes, the linear system of equations is as

$$\sum_{k=1}^{N} C_k \mu_k + \sum_{j=1}^{N_W} C_j \mu_{W,j} - \sum_{k=1}^{N} B_k \mu_k = 0 \qquad (30)$$

where the C_k, C_j, and B_k are the potential influence coefficients of body doublet, wake doublet, and body source, respectively. However, due to a large influence of wake for rotorcraft aerodynamics (Ref. 18), the wake model is essential to accurately predict the aerodynamic performance of rotor blades. In this study, the wakes are modeled by Lagrangian description of Navier-Stokes equation, and the vorticity field is as

$$\omega(x,t) = \sum_{j=1}^{N} \xi_\sigma(x - x_j)\alpha_j = \sum_{j=1}^{N} \xi_\sigma(x - x_j)\omega_j V_j \quad (31)$$

where x_j and α_j are the position of particle and total vorticity inside the vortex particle, respectively. V_j is the particle volume. The position of particles will be updated using convection velocity over all the particles. In the hybrid method, the particle influence is added into the freestream conditions to solve for the strength of source for each panel (Ref. 13).

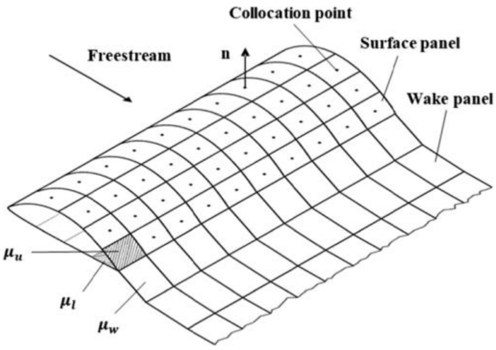

Figure 3: Surface and wake panel arrangements on the blade (Ref. 11)

As shown in Figure 3, the panel method is used to simulate the rotor blade surfaces and near wake, and vortex particle method is used to model the far wake.

2.4. Aeroelastic coupling method

In this study, the aeroelastic analysis is performed by applying the loose coupling method. The following process iterates until structural nonlinear behavior is converged.

First, the aerodynamic solver predicts pressure distributions upon the blade surface, and they are transformed into normal, chordwise, and axial surface tractions in the global frame. The aerodynamic forces are then distributed over the surface nodes of structural mesh. Next, the structural solver predicts the nonlinear displacement field according to the aerodynamic force and inertial force. And the displacements are distributed over the surface nodes of aerodynamic penal. To transfer the aerodynamic forces or displacements between each solver, the interface is implemented by using a radial basis function interpolation (Ref. 19).

In aerodynamic solver, the trim is controlled via collective pitch input to satisfy the target thrust, rolling moment, and pitching moments of rotor blades in hover flight condition using the Newton-Raphson method (Ref. 20).

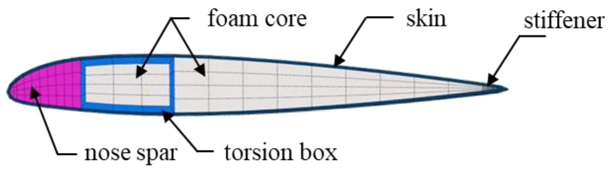

(a) internal structure

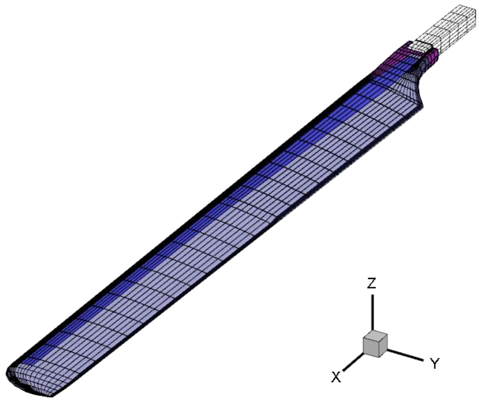

(b) FE model of MPUH blade

Figure 4: Configuration of MPUH blade

3. NUMERICAL RESULTS

3.1. MPUH

The MPUH blade developed by KARI is used to validate the structural solver. Figure 4 shows the blade internal structure and finite element (FE) modeling of MPUH rotor blade, respectively. The internal structure is composed of the nose spar, torsion box, skin, foam core, and trailing edge stiffener. The spar and trailing edge stiffener are applied to the unidirectional glass fiber, and the skin and torsion box are applied to the carbon fabric to include the proper stack angle of laminas, respectively. The number of elements and nodes from the FE discretization of MPUH blade are 6,645 and 30,489, respectively. Moreover, the total problem size is approximately 91,500 degrees of freedom.

To represent composite materials without increasing the degrees of freedom due to modeling of each lamina, the classical laminate plate theory (CLPT) method is employed. It calculates an anisotropic

constitutive matrix for a composite laminate composed of multiple plies of orthotropic material.
The prediction presented in this paper is compared to experimental data for sectional load tests and aeroelastic analysis results using CAMRAD II (Ref. 21). The sectional load tests evaluate the flap and lag moments of blades according to static loads. The aeroelastic analysis results are for hover flight conditions, with the trim target being thrust and zero rolling and pitching moments.

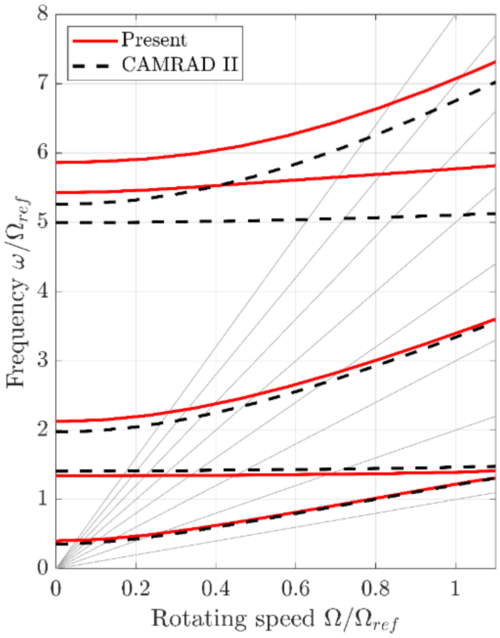

Figure 5: Rotating frequencies for MPUH blade

3.2. Dynamic characteristics of rotor blade

Figure 5 shows rotating frequencies in a vacuum for MPUH according to the rotating speed from $\Omega/\Omega_{ref} = 0.1$ to $\Omega/\Omega_{ref} = 1.1$. The present results solver is compared with those obtained by CAMRAD II. Below the third mode, the results show good agreement compared with both CAMRAD II, though there are discrepancies from CAMRAD II for modes above the fourth.
Difference between CAMRAD II and present solver is due to the nature of structural models. The beam-based solver tunes the equivalent root spring with empirically determined stiffness all the root components, whereas the present model considers each part of root components. Moreover, due to the absence of torsion bearing in our FE modeling, the fourth modes according to rotating speed show discrepancies compared to CAMRAD II.

3.3. Sectional load tests

For verification of the sectional loads calculated by force balance method employed in this study, they are compared with experimental data (Ref. 14). For sectional load tests, MPUH blade with clamped boundary condition has arbitrary rotation angle to decouple the flap and lag moments of cross section to be evaluated. It is subject to static loads of up to 6 kgf, i.e., flap and lag bending moments, and three cross sections are considered.

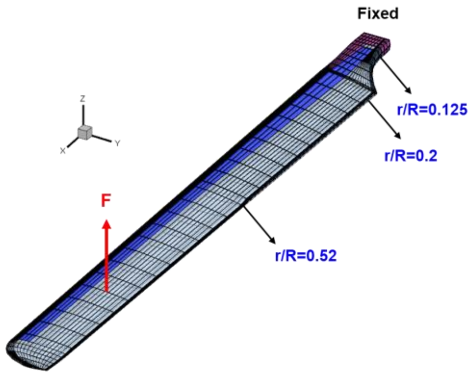

Figure 6: Description of static analysis and FE model to evaluate the flap moment

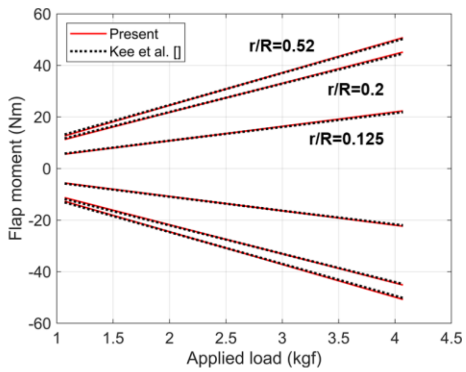

(a) Flap moment

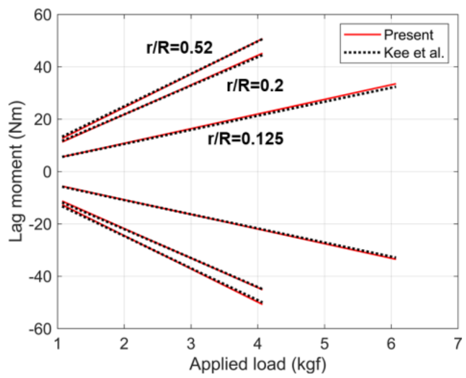

(b) Lag moment

Figure 7: Comparison of flap and lag moment under various static loads at r/R=0.125, 0.2, and 0.52

The blade model without hub is considered to depict the experiment environment. It is discretized with 20-nodes elements and the number of elements and nodes are 6,560 and 29,989, respectively. It is supported at the root surface and is subjected to a transverse static load at r/R=0.72. Moreover, to evaluate the positive and negative moment direction, the static loads is applied to transverse static loads in the positive and negative z-direction. The radial location r/R=0.125, 0.2, and 0.52. is considered to verify the method. The relevant configuration and boundary conditions are shown in Figure 6.

The flap and lag moments are calculated at the elastic center of cross sections. Figure 7 compares the experiment data (black dashed line) to calculated sectional loads using the internal forces at each node (red solid line). It shows that the results show good agreement within a relative error of 3.2%.

3.4. Aeroelastic analysis

In this study, the aeroelastic analysis in hover flight condition is performed and compared to CAMRAD II results for MPUH blade. The blade surface interacting between structural and aerodynamic solver is defined in range of r/R=0.3~1. The rotor blade is trimmed to reach the target thrust using the Newton-Raphson iteration method. Four thrust conditions are considered from high to low thrust condition. The trimmed parameters are collective, longitudinal, and lateral angles and the target thrusts are listed in Table 1.

Table 1: Target thrust and trimmed collective angle

No.	Thrust (N)	Trimmed collective (°)	
		Present	CAMRAD II
1	500	2.75	2.23
2	1,000	5.06	5.41
3	1,500	7.06	7.08
4	2,000	8.97	9.01

Prediction of lift and drag distributions are shown in Figure 8. There are discrepancies between the present aerodynamic solver and CAMRAD II results at the inboard of blade. It is because of the modeling of blade hub and root. Specifically, the downwash induced by rotor wake near the inboard of blade affect the effective angle of attack, which causes the decrease of lift and drag coefficients. Thus, it can be found that the lift coefficients near the inboard of blade (r/R = 0.2~0.5) decrease more when lower thrust condition is considered.

The displacements evaluated at r/R=0.95 are shown in Figure 9, and those are compared with the CAMRAD II results. The results show discrepancies for each case, but they capture similar trends as the thrust increases.

The blade sectional loads referred to each directional force, bending and torsion moments are examined. Figure 10 shows the sectional forces and moments at r/R=0.125, 0.2, and 0.52. The solid line and dash line are the present and CAMRAD II results, respectively. The black (case 1), red (case 2), blue (case 3), and magenta (case 4) lines represent each trimmed case. Figure 11 shows the sectional forces and moments along the spanwise direction for the highest thrust case (5,000N). The present results show similar trends along to the spanwise direction when compared to the CAMRAD II results.

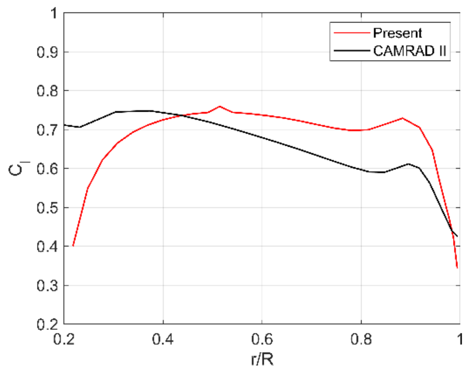

(a) Lift coefficient

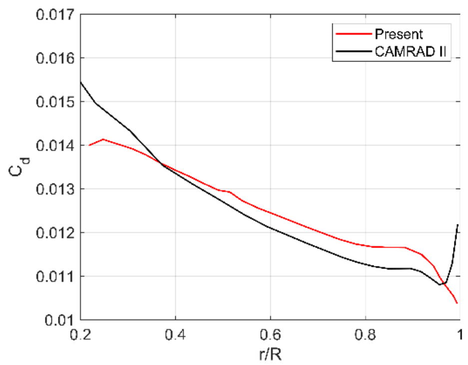

(b) Drag coefficient

Figure 8: C_l and C_d coefficients along the spanwise for MPUH blade for the highest thrust condition

Moreover, one of the benefits of 3D FEM-based analysis is the prediction of stress distribution with respect to the blade components such as spar and torsion box. The axial stress (σ_{11}) and equivalent stress (σ_{von}) distribution within the blade in hover flight condition are shown in Figure 12 and 13.

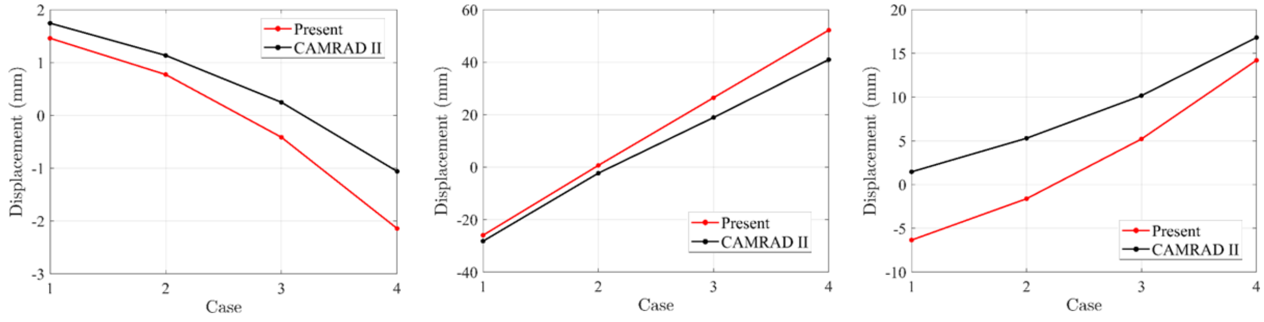

(a) Axial displacement (b) Flap displacement (c) Lag displacement

Figure 9: Comparison of the tip deflection according to the thrust condition

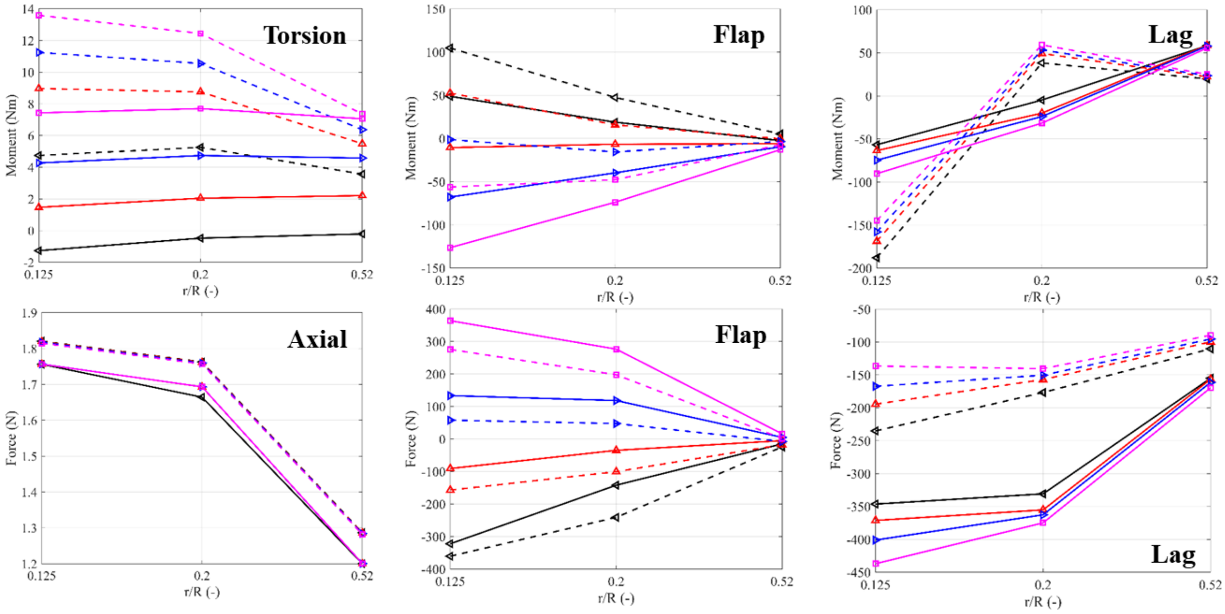

Figure 10: Comparison of sectional loads according to the thrust condition

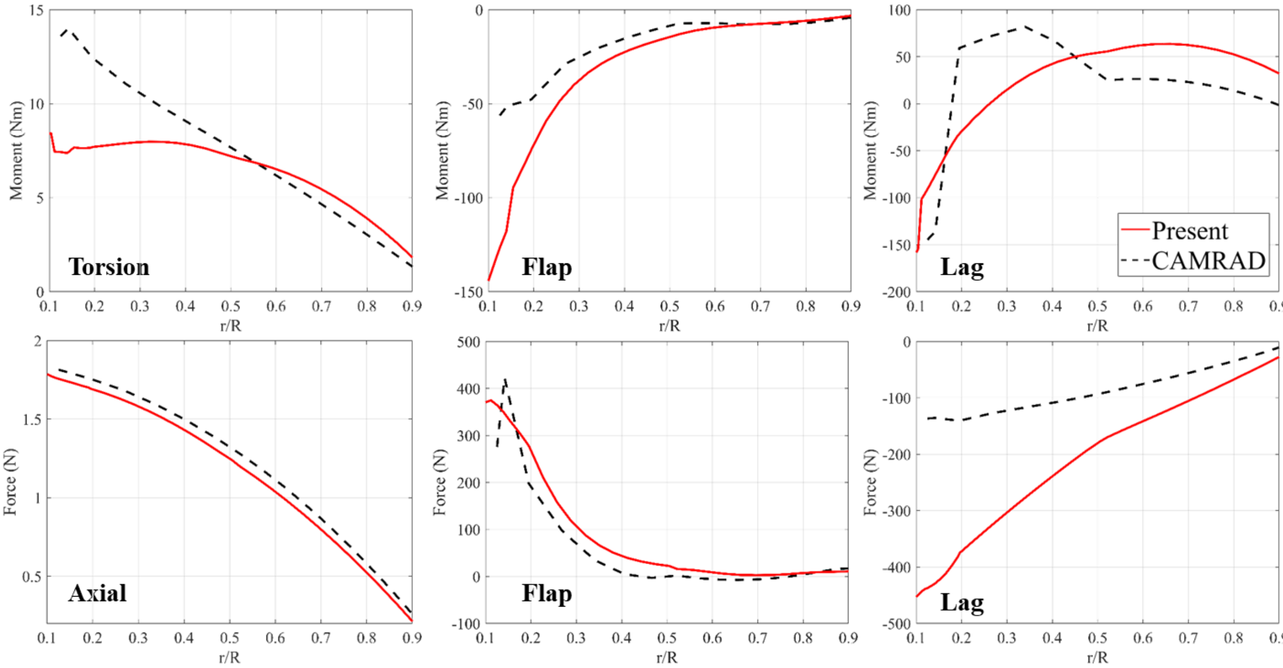

Figure 11: Comparison of spanwise sectional loads (T = 2,000N)

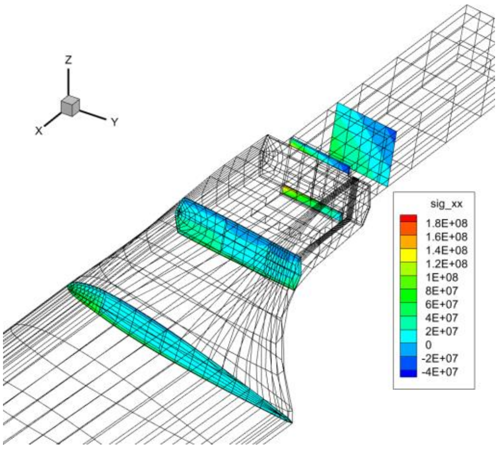

(a) axial stress, σ_{11}

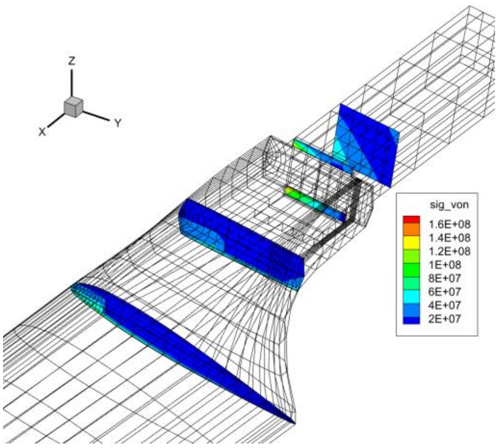

(b) Equivalent stress σ_{von}

Figure 11: Blade axial stress σ_{11} and equivalent stress σ_{von} at the highest thrust case (T = 2,000N)

Examination of the cross sections reveals that the blade spar significantly takes the centrifugal and aerodynamic loads, but there appears to be some stress carried by the blade torsion box. Moreover, there appears to be stress concentration near the bolted joint of blade. Since the behavior of the blade dominates the flap motion, the tensile stress and compressive stress appear near upper and lower surface of blade, respectively.

4. CONCLUSIONS

This study presents the aeroelastic analysis of single rotor blade by coupling 3D finite element analysis with panel/vortex particle hybrid method. The updated Lagrangian formulation is used to describe the nonlinear behavior of blade and the rotating effect such as spin-softening and centrifugal effect are considered. Moreover, the force balance method is used to calculate the sectional loads of rotor blade.

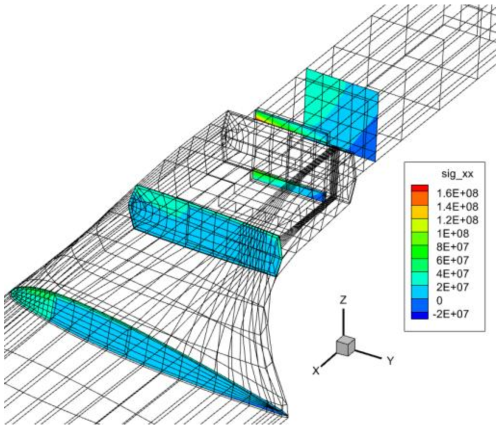

(a) axial stress, σ_{11}

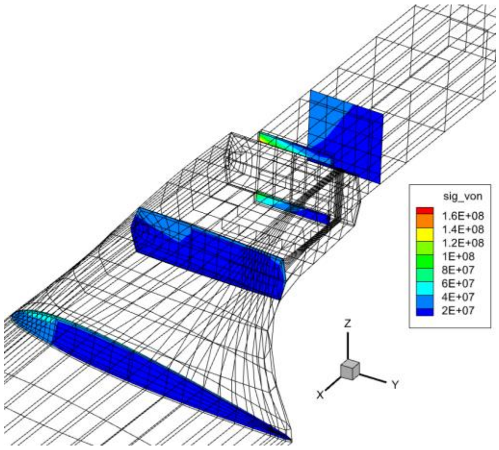

(b) Equivalent stress σ_{von}

Figure 12: Blade axial stress σ_{11} and equivalent stress σ_{von} at the lowest thrust case (T = 500N)

The FE model of MPUH blade is developed and is used to perform sectional loads tests and aeroelastic analysis. The static loads were applied to consider the flap and lag moments, and the results matched well compared with the experimental data. Through the loose coupling method, the aeroelastic analysis coupled with panel/vortex particle hybrid method was performed to predict the performance of blades in hovering condition. The prediction of airloads, displacement and sectional loads show discrepancies compared with CAMRAD II results, but can capture the similar trends along the spanwise direction. Moreover, predictions of the distributed 3D stress field are presented.

In the future, the flexible multibody dynamics will be applied to model the control system including the pitch bearing and pitch link etc. Moreover, the aeromechanical analysis in forward flight condition will be performed.

Author contact:

Seongwoo Cheon chsu0725@jbnu.ac.kr

Byeongju Kang kbj0862@jbnu.ac.kr

Sangmin Son 2017011848@gnu.ac.kr

Salang Lee leelove6045@gnu.ac.kr

Haeseong Cho hcho@jbnu.ac.kr

Hakjin Lee hlee@gnu.ac.kr

Youngjung Kee naltlguy@kari.re.kr

5. ACKNOWLEDGMENTS

This work was supported by Korea Research Institute for defense Technology planning and advancement (KRIT) grant funded by the Korea government (DAPA (Defense Acquisition Program Administration)) (No. KRIT-CT-22-082, Design/Manufacturing Technology of Rigid Coaxial Rotor System for High-Speed Compound Helicopter, 2024)

6. REFERENCES

1. Hodges, D.H. and E.H. Dowell, *Nonlinear equations of motion for the elastic bending and torsion of twisted nonuniform rotor blades.* No. A-5711. 1974.

2. Hodges, D.H., *A mixed variational formulation based on exact intrinsic equations for dynamics of moving beams*. International journal of solids and structures, 1990. 26(11): p. 1253-1273.

3. Staruk, W., Datta, A., Chopra, I., & Jayaraman, B. (2018). *Integrated three-dimensional aeromechanics analysis of the NASA tilt rotor aeroacoustic model*. Journal of the American Helicopter Society, 63(3), 1-12

4. Yeo, H., K.-V. Truong, and R. Ormiston. *Assessment of 1-D versus 3-D methods for modeling rotor blade structural dynamics*. in 51st AIAA/ASME/ASCE/AHS/ASC Structures, Structural Dynamics, and Materials Conference 18th AIAA/ASME/AHS Adaptive Structures Conference 12th. 2010.

5. Truong, K., H. Yeo, and R.A. Ormiston. *Investigation of finite element approaches for rotor blade structural dynamics*. in Proceedings of the 36th European Rotorcraft Forum. 2010.

6. Kee, Y.J. and S.J. Shin, *Structural dynamic modeling for rotating blades using three dimensional finite elements*. Journal of Mechanical Science and Technology, 2015. 29: p. 1607-1618.

7. Datta, A. *X3D—A 3D Solid Finite Element Multibody Dynamic Analysis for Rotorcraft.* in American Helicopter Society Technical Meeting on Aeromechanics Design for Vertical Lift. 2016. Vertical Flight Soc. San Francisco.

8. Datta, A., & Johnson, W. (2014, May). *Integrated Aeromechanics with Three-Dimensional Solid-Multibody Structures*. In American Helicopter Society Annual Forum and Technology Display (No. ARC-E-DAA-TN14323).

9. Patil, M., & Datta, A. (2022). *Three-dimensional aeromechanical analysis of lift-offset coaxial rotors*. In AIAA SciTech 2022 Forum (p. 0928).

10. Staruk, W., & Datta, A. (2019). *Gimbaled tiltrotor conversion flight loads prediction using three-dimensional structural analysis*. Journal of Aircraft, 56(2), 758-770.

11. Lee, H., Sengupta, B., Araghizadeh, M. S., & Myong, R. S. (2022). *Review of vortex methods for rotor aer-odynamics and wake dynamics*. Advances in Aerodynamics, 4(1), 20.

12. Masarati, P.; Morandini, M.; Mantegazza, P. *An Efficient Formulation for General-Purpose Multibody/Multiphysics Analysis*. J. Comput. Nonlinear Dyn. 2014, 9, 041001

13. Zhu, W., Morandini, M., & Li, S. (2021). *Viscous vortex particle method coupling with computational struc-tural dynamics for rotor comprehensive analysis*. Applied Sciences, 11(7), 3149.

14. Kee, Y.J., D.K. Kim, and J.W. Shin, *Cross-sectional Design and Stiffness Measurements of Composite Rotor Blade for Multipurpose Unmanned Helicopter*. Journal of Aerospace System Engineering, 2019. 13(6): p. 52-59.

15. Bathe, K.J., *Finite element procedures*. 2006: Klaus-Jurgen Bathe.

16. Kim, N.H., *Introduction to nonlinear finite element analysis*. 2014: Springer Science & Business Media.

17. Im, B., et al., *Geometrically exact beam analysis based on the exponential map finite rotations*. International Journal of Aeronautical and Space Sciences, 2020. 21: p. 153-162.

18. Leishman, G.J., *Principles of helicopter aerodynamics with CD extra*. 2006: Cambridge university press.

19. Cho, H., et al., *Extensive 3D analysis for fluid–structure interaction of spanwise flexible plunging wing 3D FSI Analysis for Spanwise Flexible Plunging Wing*. The Aeronautical Journal, 2019. 123(1262): p. 484-506.

20. Johnson, W., *Rotorcraft aeromechanics*. Vol. 36. 2013: Cambridge university press.

21. Johnson, W. *Technology Drivers in the Development of CAMRAD II*. in American helicopter society aero-mechanics specialists conference, San Francisco, California. 1994.